Available online at www.sciencedirect.com
ScienceDirect
Journal of Computational Physics 227 (2007) 279–291
JOURNAL OF COMPUTATIONAL PHYSICS
www.elsevier.com/locate/jcp

A continuum–atomistic simulation of heat transfer in micro- and nano-flows

Jin Liu [a,*], Shiyi Chen [a,b], Xiaobo Nie [c,d], Mark O. Robbins [a,c]

[a] Department of Mechanical Engineering, The Johns Hopkins University, Baltimore, MD 21218, USA
[b] CoE and CCSE, Peking University, Beijing, China
[c] Department of Physics and Astronomy, The Johns Hopkins University, Baltimore, MD 21218, USA
[d] Materials and Construction Research Division, National Institute of Standards and Technology, Gaithersburg, MD 20899, USA

Received 22 December 2006; received in revised form 12 June 2007; accepted 25 July 2007
Available online 2 August 2007

Abstract

We develop a hybrid atomistic–continuum scheme for simulating micro- and nano-flows with heat transfer. The approach is based on spatial "domain decomposition" in which molecular dynamics (MD) is used in regions where atomistic details are important, while classical continuum fluid dynamics is used in the remaining regions. The two descriptions are matched in a coupling region where we ensure continuity of mass, momentum, energy and their fluxes. The scheme for including the energy equation is implemented in 1-D and 2-D, and used to study steady and unsteady heat transfer in channel flows with and without nano roughness. Good agreement between hybrid results and analytical or pure MD results is found, demonstrating the accuracy of this multiscale method and its potential applications in thermal engineering.

Keywords: Continuum–atomistic multi-scale simulation; Heat transfer; Domain decomposition; Hybrid method; Micro/nano fluidics

1. Introduction

Heat transfer in micro- and nano-fluidic devices is important to many engineering applications [1–3]. However, calculating the behavior of such devices poses a great challenge. As system dimensions shrink to small scales, the assumptions of continuum hydrodynamics break down. In particular, the molecular mean free path may no longer be negligible and macroscopic constitutive relations and boundary conditions become inadequate. In principle, this problem can be resolved by using a fully atomistic description such as molecular dynamics (MD) simulations. However, MD simulations on current computers are typically limited to dimensions less than 100 nm and times much shorter than a microsecond. Thus they can not treat most systems of experimental interest.

* Corresponding author.
E-mail address: jliu36@jhu.edu (J. Liu).

0021-9991/$ - see front matter
doi:10.1016/j.jcp.2007.07.014

In recent years, a new class of hybrid approaches has been developed that combines the strengths of atomistic and continuum approaches. They are based on the observation that the breakdown of the continuum description is primarily confined to small spatial regions, for example near fluid–fluid or fluid–solid interfaces. An atomistic description is required in these regions, but the remaining bulk regions can be described with less computationally intensive continuum equations. The key difficulty is in constructing algorithms for coupling the very different continuum and atomistic descriptions at their interface.

Early coupling schemes included fluid flux but not heat transfer. O'Connell and Thompson [4] coupled atomistic and continuum simulations at opposite ends of an overlap region. The mean atomistic velocity at the end of the atomistic region was constrained to follow the continuum solution using a relaxation method. The main limitation of their approach was that it did not allow mass flux between atomistic and continuum regions. This has been overcome in several ways in subsequent work. Hadjiconstantinou et al. [5] developed a Maxwell Demon method to simulate incompressible flow and used a Schwarz iteration method to ensure the consistency of MD and continuum descriptions. Results from their approach for steady channel flow with an obstacle [5] and the moving contact line problem [6] are consistent with full MD simulations. Ren et al.[15] proposed a general multi-scale method for micro-fluidics. In their scheme, a macroscopic solver is adopted in the whole computational domain while the missing data, such as the flux and boundary conditions are evaluated from local MD simulations. Flekkoy et al. [7] proposed a scheme based on the continuity of mass and momentum flux for simulating isothermal, compressible flow. More recently, Nie et al. [13] developed a robust hybrid model based on"constrained dynamics" for simulating incompressible flows. They successfully applied the method to explore the physics at singular points in driven cavity flows [14,16]. With the aid of multi-grid techniques, they were able to resolve flows from molecular to millimeter scales [16].

Recent work has extended hybrid methods to include heat flow. Wagner et al. generalized the work of Flekkoy et al. to include energy transfer, and verified the conservation of mass, momentum and energy in simulations of homogeneous flow [8,9]. Buscalioni et al. [10–12] adopted a similar flux coupling scheme and demonstrated their approach by simulation of transverse and longitudinal waves. Both of these approaches considered compressible flow.

In this paper, we extend the hybrid method for isothermal, incompressible flow developed in Refs. [13,14,16] to include heat transfer. In particular, "constrained dynamics" is used to couple the atomistic and continuum velocities in the momentum equations, and atomistic and continuum temperatures in the energy equations are coupled by rescaling particle velocities. The approach is tested against fully atomistic simulations of heat transfer through a fluid layer confined between flat and rough surfaces. The effect of wall-induced flows and the unsteady response to a temperature increase are also considered. In all cases, the hybrid method reproduces purely atomistic results in a small fraction of the computational time and with less noise.

The outline of the paper is as follows. In Section 2, we describe the numerical algorithm with special attention to the new features associated with the heat equation. In Section 3, we demonstrate the success of the scheme through simulations of 1D and 2D, steady and unsteady, heat transfer in channels. A brief summary and concluding remarks are presented in Section 4.

2. Numerical algorithm

2.1. Domain decomposition

Fig. 1 illustrates the general scheme of domain decomposition in our calculations. The simulation is divided into two spatial domains, the particle (atomistic) domain indicated by dots and the continuum domain represented by shading. Molecular dynamics simulations are performed in the atomistic domain, and classical continuum fluid dynamics equations are solved on a grid in the continuum domain. There is an overlap region between these two domains which typically extends a few times the continuum grid spacing. Both molecular dynamics and continuum calculations are performed in this overlap region. The key element of the algorithm

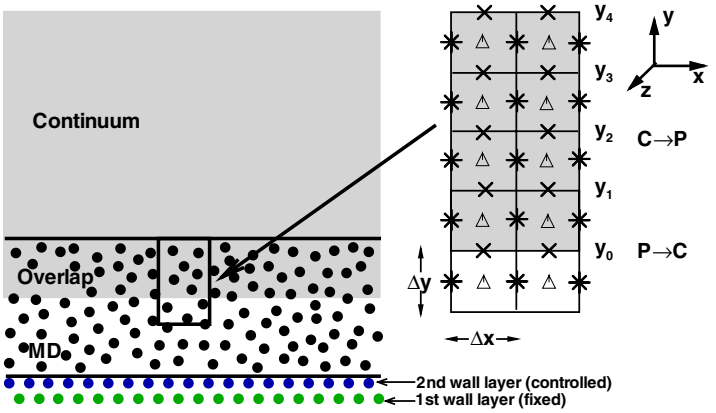

Fig. 1. Schematic of the hybrid method. The continuum description is used in the shadowed region and the atomistic description is used in the dotted region. In $C \rightarrow P$, continuum solutions provide boundary conditions for MD simulations and in $P \rightarrow C$ atomistic solutions provide boundary conditions for continuum simulations. The continuum equations are solved on a staggered grid with u_x defined at asterisks, u_y defined at crosses, and p and T defined at triangles.

is the scheme for coupling the particle and continuum solutions to ensure continuity of fluxes across the overlap region.

The MD domain in our simulations contains both a solid wall and a fluid. The interactions between fluid atoms are modeled with a truncated and shifted Lennard-Jones potential,

$$V^{\mathrm{LJ}}(r) = 4\epsilon\left[\left(\frac{\sigma}{r}\right)^{12} - \left(\frac{\sigma}{r}\right)^{6} - \left(\frac{\sigma}{r_c}\right)^{12} + \left(\frac{\sigma}{r_c}\right)^{6}\right], \tag{1}$$

where ϵ is the characteristic binding energy, and σ the atomic diameter. The interactions are truncated at $r_c = 2.2\sigma$ to reduce the computational cost. To allow comparison with previous results [4,13,14], we use the same fluid density, $\rho = 0.81 m\sigma^{-3}$, where m is the particle mass. Fluid and solid atoms also interact with a Lennard-Jones potential, but with a reduced binding energy $\epsilon_{\mathrm{wf}} = 0.75\epsilon$ that leads to a no-slip boundary condition.

Two layers of solid atoms form the wall (Fig. 1). They are arranged to form a (1 1 1) surface of an fcc crystal with the same density as the fluid. The first layer is held fixed. Atoms in the second layer are coupled to their nearest-neighbors by ideal harmonic springs with spring constant $500\epsilon/\sigma^2$. This corresponds to having interactions about nine times stronger than those within the fluid, and ensures that the crystal structure is retained.

We track the time evolution of all particle trajectories by integrating their equations of motion using the velocity Verlet scheme with time step $\Delta t_{\mathrm{MD}} = 0.005\tau$, where $\tau = (m\sigma^2/\epsilon)^{1/2}$ is the characteristic time of the Lennard-Jones potential. The wall temperature is controlled by coupling atoms in the second layer to a Langevin thermostat [17]. Their equation of motion is

$$\frac{\mathrm{d}m_i\mathbf{v}_i(t)}{\mathrm{d}t} = \mathbf{f}_i(t) - \xi m_i \mathbf{v}_i(t) + \mathbf{W}_i(t), \tag{2}$$

where $\mathbf{v}_i$ is the velocity of the ith particle and $\mathbf{f}_i(t)$ the force from other particles. The second term on the right side of Eq. (2) represents the damping force and ξ is the damping rate. The third term, $\mathbf{W}_i(t)$, is a random force sampled from a Gaussian distribution with zero mean and a standard deviation of $\sqrt{2\xi k_{\mathrm{B}} T/\Delta t_{\mathrm{MD}}}$. Here T is the desired temperature and k_{B} is Boltzmann's constant. The damping rate controls the effective thermal conductivity from the wall to the thermal bath represented by the thermostat. We use a value $\xi = 1.0\tau^{-1}$ that is small enough that solid atoms are underdamped, but large enough that the temperature increase of the wall is small. The results are relatively insensitive to changes of ξ by a factor of 2, but the temperature rise of this wall layer becomes significant at much smaller ξ (Section 3.2). In the continuum region, the following two-dimensional incompressible Navier–Stokes equations are solved,

$$\begin{aligned}
&\nabla \cdot \mathbf{u} = 0,\\
&\frac{\partial \mathbf{u}}{\partial t} + \mathbf{u}\cdot\nabla\mathbf{u} = -\frac{1}{\rho}\nabla p + \frac{\mu}{\rho}\nabla^2\mathbf{u},\\
&\frac{\partial T}{\partial t} + \mathbf{u}\cdot\nabla T = \frac{\lambda}{\rho c_v}\nabla^2 T + \frac{2\mu}{\rho c_v}\left[\left(\frac{\partial u_x}{\partial x}\right)^2 + \left(\frac{\partial u_y}{\partial y}\right)^2 + \frac{1}{2}\left(\frac{\partial u_x}{\partial y} + \frac{\partial u_y}{\partial x}\right)^2\right].
\end{aligned} \tag{3}$$

The first equation enforces incompressibility on the fluid velocity $\mathbf{u}$. In the momentum equation, p is the pressure and μ the dynamic viscosity. The final heat equation contains the specific heat c_v and thermal conductivity λ. The transport coefficients μ, c_v and λ must be consistent with the atomistic potential in order to ensure continuity in the overlap region. They are determined through preliminary MD simulations as discussed in Section 3.1.

The N–S equations are integrated using the projection method with mesh size of $\Delta x = \Delta y = 6.25\sigma$. A staggered grid [18] is implemented as illustrated in Fig. 1. Pressure and temperature are defined at the centers of cells (triangles). A Neumann boundary condition is applied in solving the pressure Poisson equation. The x and y components of the velocity are defined at the middle of the vertical (asterisks) and horizontal (crosses) edges of the cells, respectively. To ensure numerical accuracy, the continuum equations must be integrated with a time step Δt_{FD} that is much smaller than the characteristic time of flows on the scale of the grid. The characteristic times for velocity and temperature at low Reynolds number are $\rho\Delta x\Delta y/\mu = 15.2\tau$ and $\rho c_v\Delta x\Delta y/\lambda = 10\tau$, using the transport coefficients obtained in Section 3.1. The time scale on which atoms sample different kinetic energies is of order the velocity autocorrelation time $t_{\mathrm{vv}} \sim 0.14\tau$ [4]. As described below, thermal averages of atomistic quantities are evaluated on intervals of width Δt_{FD}, and choosing this larger than t_{vv} ensures that atoms sample some of their thermal distribution over the averaging interval. The simulations below used $\Delta t_{\mathrm{FD}} = 50\Delta t_{\mathrm{MD}} = 0.25\tau$. Runs with $\Delta t_{\mathrm{FD}} = 1\tau$ gave equivalent results, but little speedup since most of the compute time is in the MD domain.

2.2. Boundary conditions on continuum from particles

At the bottom of the overlap region in Fig. 1, the particle description provides boundary conditions for the continuum equations ($P \rightarrow C$). The quantities required by the continuum description are mean velocities and temperatures that are readily determined from spatial and temporal averages of particle properties. For example, the continuum equations require values of u_y at the crosses along $y = y_0$ and values of u_x at the asterisks along $y = y_0 - \Delta y/2$. These are obtained by averaging the velocities of all particles in an area Δx by Δy centered on the point of interest, over the entire period L_z in the z direction, and over a time interval Δt_{FD}.

The temperature is obtained in the center of the continuum cells. The instantaneous temperature in cell J is given by

$$k_{\mathrm{B}}T_{J,\mathrm{MD}}(t) = \frac{2}{3(N_J - 1)}\sum_{i}^{N_J}\frac{1}{2}m_i(\mathbf{v}_i - \mathbf{u}_J)^2. \tag{4}$$

where $\mathbf{u}_J$ is the mean velocity evaluated by averaging over the N_J atoms in the cell. Subtracting the mean velocity ensures that the expression has Galilean invariance and the prefactor reflects the fact that there are $3(N_j - 1)$ remaining degrees of freedom each with energy $k_{\mathrm{B}}T/2$. Note that we will consider fairly small fractional changes in T and it is important to use velocities from the velocity-Verlet algorithm to get sufficiently accurate temperatures. The temperature is averaged over Δt_{FD} before being passed to the continuum solution.

Averages of particle quantities necessarily include thermal fluctuations, while the continuum equations do not. In some cases these fluctuations may be of interest [19], but in the cases considered below our goal is to ensemble average until fluctuations become negligible. In purely atomistic simulations of steady state behavior this can be done by averaging over long time intervals but the averaging time grows rapidly with system size. The reason is that there are long-lived hydrodynamic modes associated with flow of particles and heat. For a system with dimension L, these would correspond to $\rho L^2/\mu$ and $\rho c_v L^2/\lambda$ in the low Reynolds number limit. Averages must be taken over much longer times to reduce the noise in these modes. The effect of these

long-lived modes can be reduced by considering an ensemble of independent systems, where the noise is necessarily decorrelated.

To benchmark our results we will frequently compare to purely atomistic MD simulations. In this case, results are averaged over 10 different realizations of the same physical system. These were typically run in parallel on different processors, making efficient use of a small local cluster. In the hybrid method we also consider 10 different realizations of the MD region. Their velocities and temperatures are averaged and input to a single continuum simulation. One could instead couple each atomistic simulation to a separate continuum calculation and then average the results at the end. However this generates larger statistical errors. The reason is that fluctuations in each atomistic region couple to themselves through the long-lived hydrodynamic fluctuations and only average out over longer times. Averaging the realizations before they couple to the hydrodynamic modes reduces this effect. As a result, the errorbars for purely MD simulations are always substantially larger than for the hybrid method. This represents another important advantage of the hybrid approach.

2.3. Boundary conditions on particles from continuum

One common difficulty in all atomistic/continuum coupling methods is that information about macroscopic quantities does not uniquely specify the microscopic state of particles. The goal of continuum to particle coupling is to constrain the mean particle behavior without introducing unphysical artifacts associated with the constraint or the termination of the particle domain. The overlap region helps to minimize these effects.

The mean particle velocity in each cell J is constrained to follow the continuum solution $\mathbf{u}_J$ using the method described in Ref. [13]. The constraint is derived by finding the extremum of the time integral of the Lagrangian for particles subject to the nonholonomic constraint,

$$\frac{1}{N_J}\Sigma_i \mathbf{v}_i = \mathbf{u}_J(t). \tag{5}$$

The resulting equation for particles in cell J is

$$\ddot{\mathbf{x}}_i = \frac{\mathbf{F}_i}{m} - \frac{1}{N_J m}\sum_{k=1}^{N_J}\mathbf{F}_k + \frac{\mathrm{D}\mathbf{u}_J(t)}{\mathrm{D}t}, \tag{6}$$

where $\mathbf{F}_i = -\frac{\partial}{\partial x_i}\sum_{j\neq i} V^{\mathrm{LJ}}(r_{ij})$ and $\mathrm{D}\mathbf{u}_J/\mathrm{D}t$ indicates the material derivative. The last two terms ensure that the mean particle velocity tracks the continuum solution by subtracting the sum of all forces on particles in the cell and adding the material derivative of the continuum solution. More details are provided in Ref. [13]. O'Connell and Thompson implemented a similar approach but imposed the constraint through a relaxation equation with a characteristic time constant. This introduces time delays in the coupling of continuum and particle descriptions that can alter dynamic solutions.

In the examples described below, the velocity constraint was imposed on cells between y_1 and y_3 in Fig. 1. This constraint on the mean velocity is not sufficient to prevent some particles from leaving the particle domain. To confine particles, an additional nonlinear force is applied to particles between y_3 and y_4

$$F_y = -\alpha p_0 \sigma \frac{(y-y_3)}{1-(y-y_3)/(y_4-y_3)}, \tag{7}$$

where $p_0 = 3.16\epsilon/\sigma^3$ is the equilibrium pressure corresponding to the fluid density $\rho = 0.81 m\sigma^{-3}$ and α is a constant of order one. In our simulations, $y_4 - y_3 = \Delta y$ and $\alpha = 1$. This leads to a relatively smoothly varying potential that does not introduce density oscillations that might propagate beyond the overlap region.

Werder et al. [20] have proposed an alternative confining force. By using the pair correlation function in the equilibrium fluid to construct the confining force, one can have the density of fluid atoms drop rapidly to zero without introducing density oscillations. This may be important in fluids with long range interactions and correlation lengths. Werder et al. found substantial density shifts and oscillations with other algorithms. However problems they attributed to the algorithm used here and in earlier work [13,14,16] resulted from an incorrect implementation. In particular, they did not adjust the number of particles in the simulation to give the correct density or include the buffer region above y_3. This region allows the density to be constant over the range

where continuum and atomistic solutions are coupled ($y_1 < y < y_3$). The density then decays smoothly to zero over about 1σ as y increases above y_3. The force is slowly varying over this range of y. There is a small computational cost associated with atoms in the buffer region, but it is negligible for the short-range interactions considered here. The buffer region is also helpful in equilibrating atoms that are added to the system as described next. To maintain mass conservation, the particle flux across $y = y_3$ is calculated based on the continuum velocity field. The change in number of atoms in a cell in $\Delta t_{\mathrm{FD}}/m$ is

$$\Delta n = -A\rho u_y \Delta t_{\mathrm{FD}}/m, \tag{8}$$

where $A = \Delta x \Delta z$ is the area of the cell surface. The change in number is integrated until its magnitude exceeds an integer n'. Then if the flux is negative, the n' atoms closest to y_4 are removed. If n' is positive, n' atoms are inserted at evenly spaced times over the following Δt_{FD}. The fractional remainder is added to the flux at the next time interval. Particles are inserted at random positions in the $x - z$ plane and 1σ above the particle in the cell that has the largest y (always well below y_4). The initial velocity of an inserted particle is equal to the continuum velocity in the corresponding cell. The peculiar velocities of atoms in the buffer region between y_3 and y_4 are coupled to a Langevin thermostat. The set temperature is the continuum solution extrapolated to y_3 and $\xi = 1\tau^{-1}$. This insures that atoms entering the coupling region are properly thermalized. To constrain the particle temperature to the continuum solution for $y < y_3$, we used a simple velocity rescaling algorithm that is also used in standard MD simulations [21]. At each time step, the particle temperature in a cell is calculated from Eq. (4). The velocities are then rescaled so that the microscopic temperature $T_{J,\mathrm{MD}}$ equals the set temperature from the continuum solution $T_{J,\mathrm{C}}$:

$$\mathbf{v}_i = \mathbf{u}_J + \sqrt{\frac{T_{J,\mathrm{C}}}{T_{J,\mathrm{MD}}}}(\mathbf{v}_i - \mathbf{u}_J). \tag{9}$$

Note that it is important to rescale only the thermal fluctuations around the mean velocity $\mathbf{u}_J$.

One of the weaknesses of velocity rescaling thermostats is that they remove the intrinsic fluctuations between kinetic and potential energy [21]. As discussed in the next subsection, the temporal fluctuations in kinetic energy are directly related to the specific heat and are substantial in small systems. Our use of relatively large cells reduces artifacts associated with maintaining a strictly constant kinetic energy and the thermostat is only applied in the outer part of the overlap region. Other thermostats were also considered, but all introduce an additional time lag over which the temperature is controlled. While this was not a problem in steady state simulations, it affected dynamic simulations. Combining velocity rescaling with the constraint equation (Eq. (6)) removes all time delays in the coupling algorithm.

The impact of velocity rescaling on our simulations was minimized by applying it to relatively large volumes $\Delta x \Delta y \Delta z$. In addition, applying rescaling at a distance from the edge of the continuum region that is larger than the correlation length ensures that spurious oscillations decay before reaching the purely atomistic region. In our simulations the rescaling was only applied in the upper $2\Delta y$ of the MD region between y_1 and y_3 (Fig. 1). The spatial separation between the thermostatted region ($y > y_1$) and the region that constrains the continuum solution ($y < y_0$) plays another important role. The separation ensures that both continuum and atomistic systems have a heat flux determined by the temperature difference between $y_0 - \Delta y$ and $y_1 + \Delta y$. The two fluxes are equal on average if the continuum conductivity is correctly fit to the response of the particles. In contrast, if the thermostat is applied down to y_0, the atomistic and continuum heat flux can differ due to the flow of heat to the thermostat. This produced a small difference between the temperature derivatives in MD and continuum regions in plots like Figs. 2 and 3b.

3. Results and discussion

3.1. Determination of fluid transport coefficients

As noted above, the bulk fluid transport coefficients in Eq. (3) must be consistent with transport in the atomistic region in order to ensure continuity across the overlap region. The dynamic shear viscosity μ, thermal conductivity λ and the heat capacity c_v were determined from equilibrium MD simulations with $N = 4096$

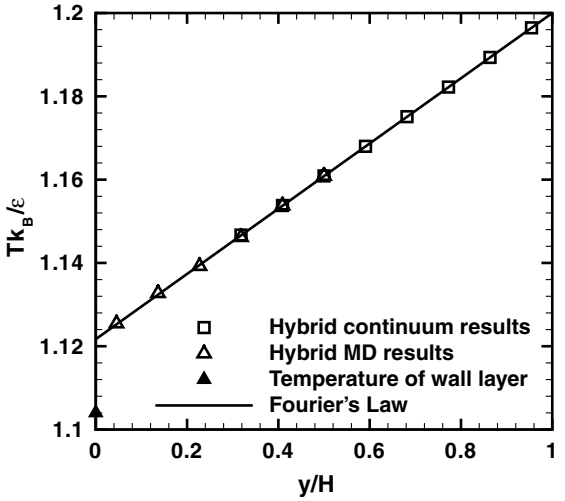

Fig. 2. Steady state temperature profile from a hybrid simulation of heat flux between stationary walls. Squares are from the continuum region, triangles represent MD results, and the filled triangle represents the temperature of the bottom solid wall. A straight line shows the prediction of Fourier's law. The results were averaged over 3000τ at steady state and ten independent MD runs to reduce thermal fluctuations. Statistical errors are smaller than the symbol size.

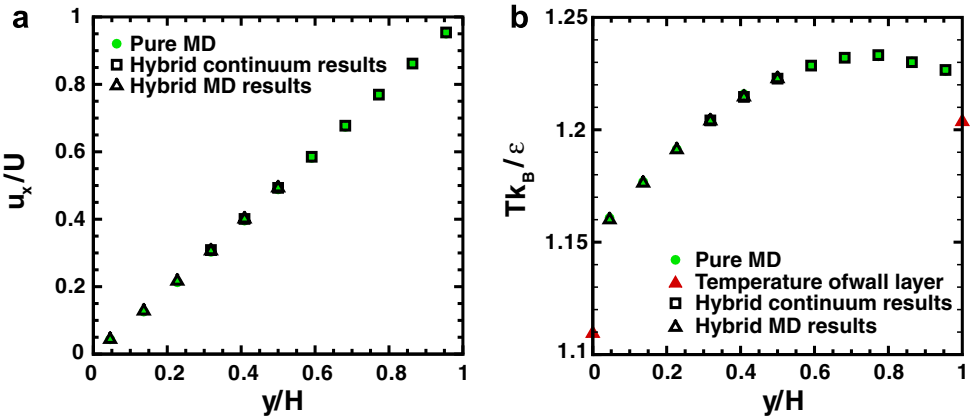

Fig. 3. Comparison of steady state (a) velocity and (b) temperature profiles from hybrid (open symbols) and pure MD (filled symbols) simulations for a moving top wall. The results were averaged over 3000τ at steady state and ten independent runs to reduce thermal fluctuations. Statistical errors are smaller than the symbol size.

particles at $\rho = 0.81m\sigma^{-3}$. The simulation domain had periodic boundary conditions with periods $L_x = 16.7\sigma$, $L_y = 19.3\sigma$, $L_z = 15.7\sigma$ along x, y and z, respectively. In principle the transport coefficients should be parameterized as a function of temperature. However, they vary slowly with temperature, and the temperature in most of our simulations only varies between $1.1\epsilon/k_B$ and $1.2\epsilon/k_B$. Thus we evaluated the coefficients at the intermediate temperature of $1.16\epsilon/k_B$. After the system equilibrated at this T, an MD run of 4×10^6 steps was performed. The kinetic energy, shear stress q_{xy} and microscopic heat current $\mathbf{j}$ were stored for each time step and used to evaluate coefficients as described below.

The heat capacity c_v can be evaluated directly in the microcanonical ensemble as

$$c_v = \frac{3k_B}{2m}\left[1 - \frac{2N}{3(k_BT)^2}\langle(\delta E_k)^2\rangle\right]^{-1}, \tag{10}$$

where T is the temperature evaluated from the average kinetic energy per particle E_k (Eq. (4)), δE_k is the deviation from this average, and the angular bracket denotes the ensemble average. This equation gave $c_v = 2.43 k_B/m$ for the heat capacity of the fluid.

The shear viscosity μ and the thermal conductivity λ can be evaluated from the same simulation using the Green-Kubo formulas [22]. The shear viscosity is related to the time correlation function of the shear stress q_{xy},

$$\mu = \frac{V}{k_B T}\int_0^\infty \langle q_{xy}(0)\cdot q_{xy}(t)\rangle \mathrm{d}t, \tag{11}$$

where V is the volume and the quantity in brackets is the autocorrelation function of the shear stress. The microscopic expression for the components of the stress tensor is

$$q_{\alpha\beta} = -\frac{1}{V}\left[\sum_i m_i v_{i\alpha} v_{i\beta} + \frac{1}{2}\sum_{i,j,i\neq j} r_{ij\alpha} F_{ij\beta}\right], \tag{12}$$

where $\mathbf{r}_{ij}$ is the vector between particles i and j, $\mathbf{F}_{ij}$ the force between them, and α and β indicate the x, y or z component.

The corresponding Green-Kubo formula for the thermal conductivity λ is

$$\lambda = \frac{V}{3k_B T^2}\int_0^\infty \langle \mathbf{j}(0)\cdot \mathbf{j}(t)\rangle \mathrm{d}t, \tag{13}$$

where the microscopic heat current $\mathbf{j}$ is given by

$$\mathbf{j}(t) = \frac{1}{V}\left[\sum_i \mathbf{v}_i \varepsilon_i + \frac{1}{2}\sum_{i,j,i\neq j} \mathbf{r}_{i,j}(\mathbf{F}_{ij}\cdot \mathbf{v}_i)\right] \tag{14}$$

and the site energy ε_i is

$$\varepsilon_i = \frac{1}{2} m_i |\mathbf{v}_i|^2 + \frac{1}{2}\sum_j V^{\mathrm{LJ}}(r_{ij}). \tag{15}$$

Based on our simulation results, the shear viscosity is $\mu = 2.08\epsilon\tau\sigma^{-3}$ and the thermal conductivity is $\lambda = 7.7 k_B/\sigma\tau$ with errorbars smaller than the last significant digit. These results are consistent with values obtained from nonequilibrium simulations in Refs. [4,23] and are used in the following hybrid simulations.

3.2. Steady flow

3.2.1. 1D channel flow without roughness

As a first demonstration of our scheme, we simulate 1D heat transfer between flat parallel walls. The fluid is confined between stationary solid walls at $y = 0$ and $y = H = 68.8\sigma$, and periodic boundary conditions with period $L_x = 18.8\sigma$ and $L_z = 4.82\sigma$ are imposed along x and z, respectively. As mentioned above, the simulation domain consists of three regions. The continuum equations (Eq. (3)) are solved for $y > 18.8\sigma$ and atomistic simulations are performed for $y < 43.8\sigma$. The two regions overlap over the central region of width $4\Delta y = 25.0\sigma$. The continuum region could of course be extended without significant computational effort but it is kept small to allow comparison to purely atomistic simulations.

The bottom and top walls were thermostatted at temperatures $1.1\epsilon/k_B$ and $1.2\epsilon/k_B$, respectively. After the simulation reached steady state, we averaged results over an additional 3000τ. Ten independent simulations in the MD region were used to further reduce statistical fluctuations. The steady state temperature distribution is shown by the open symbols in Fig. 2. Note the excellent agreement of results from the continuum region (squares) and particle region (triangles). The results follow the linear temperature profile predicted by Fourier's law of heat conduction. We would like to emphasize that the perfect matching of the temperature distribution with Fourier's Law implies that both the temperature and heat flux in the overlap region have a smooth transition, which is exactly the goal of the multiscale method.

The temperature of the bottom solid wall is also shown in Fig. 2. Note that it is slightly higher than the thermostat temperature. This reflects the finite thermal conductivity between wall atoms and the thermostat. As noted in Section 2.1, increasing the damping rate ξ, facilitates heat flow and lowers the temperature rise of the wall. There is a much larger temperature jump at the interface between fluid and solid. This reflects the Kapitza resistance for thermal flow across the interface between phases [24,25]. One of the goals of multiscale simulations with heat flux is to capture the dependence of this resistance on atomistic effects, and this can readily be done using our approach.

In the second example, we kept the same wall temperatures but moved the top wall at fixed velocity $U = 1\sigma/\tau$ to the right. Purely atomistic simulations were performed to validate the results and these also provided the appropriate boundary conditions for the continuum solution in the hybrid calculation. The no-slip condition is satisfied at the top wall, but there is a temperature jump due to the Kapitza resistance. Rather than including the Kapitza resistance [24,25] explicitly in the continuum calculation, we used the atomistic temperature profile to determine the appropriate temperature boundary condition on the top wall. A better solution would be to use atomistic simulations near both top and bottom walls, as is done in Section 3.3. Both MD and hybrid simulations were run for 3000τ after reaching equilibrium and averaged over ten independent MD runs.

Fig. 3a shows the steady state streamwise velocity distribution for both hybrid (open symbols) and pure MD (filled symbols) results. Excellent agreement between the velocity distributions is achieved. Fig. 3b presents the temperature distribution along the y direction. The small deviations between the methods are within the statistical errors, which are comparable to the symbol size for pure MD results and smaller for the hybrid method. In contrast to the results for stationary walls, the temperature distribution is nonlinear. Heat is produced almost uniformly across the fluid by viscous dissipation. Flow of this heat to the wall produces an extra parabolic contribution to the temperature profile [26].

3.2.2. 2-D heat transfer with nano roughness

To further test the applicability of our hybrid scheme, we simulate heat transfer in a more complicated system. As shown in Fig. 4, nanoscale roughness is added to the bottom wall. The lattice structure of the wall is extended to make a square bulge of side length 6.25σ centered at $x = 0.5L_x$, with $L_x = 56.3\sigma$. All other parameters are the same as in the previous section. As there, pure MD simulations were first performed for comparison. The fluid temperature at the top wall was obtained by extrapolating these results, and used as the boundary condition for the continuum region of the hybrid calculation. Fig. 5a–c show the temperature distributions along the y direction at three locations along x for stationary walls. Hybrid and pure MD results are represented by open triangles and squares respectively. All the results were obtained by averaging over 5000τ after reaching the steady state and over ten independent runs. As illustrated in Fig. 5, the hybrid results agree very well with the full MD results.

Simulations were also performed with the top wall sliding at $U = 1\sigma/\tau$ while the bottom wall was kept stationary. Figs. 6 and 7 present the comparison between hybrid and pure MD results. Fig. 6a–c show the velocity distributions at specific locations along x. The hybrid results are indicated by triangles and MD results by squares. The temperature distributions at the same locations along x are shown in Fig. 7. Deviations between the two methods are within the statistical errors, which are larger for T and for the pure MD results. Purely continuum calculations with a fixed Kapitza resistance do not reproduce these results for rough walls.

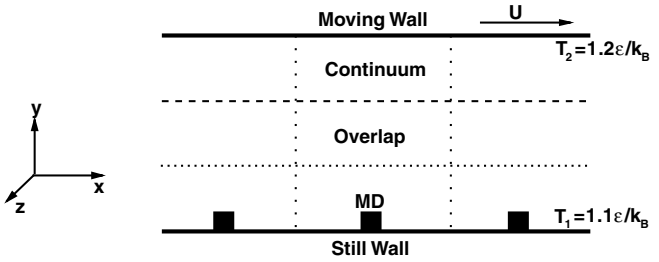

Fig. 4. Schematic of the hybrid simulation domain for channel flow with a rough bottom wall. There is one square bump of edge 6.25σ per period $L_x = 56.3\sigma$ along x.

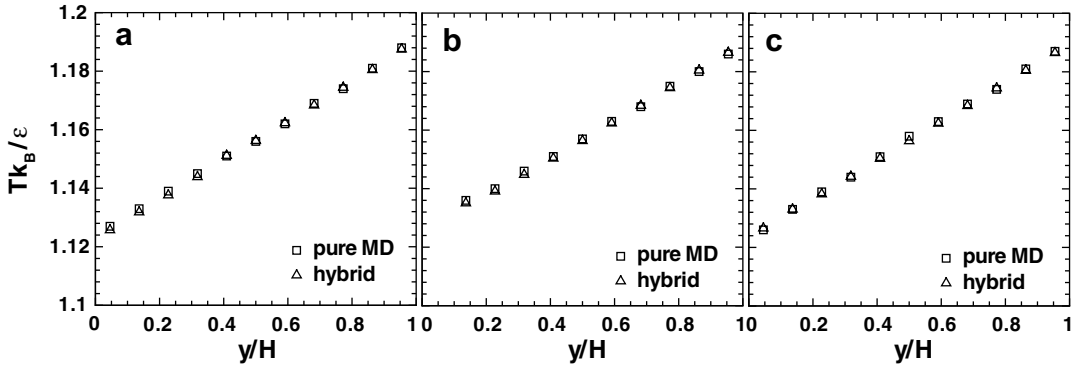

Fig. 5. Comparison of hybrid (triangles) and purely atomistic (squares) results for the steady state temperature distribution above a stationary rough wall as a function of y at (a) $x = 0.28L_x$, (b) $x = 0.5L_x$ and (c) $x = 0.72L_x$. The results were averaged over 5000τ at steady state and ten independent runs to reduce thermal fluctuations. Errorbars are smaller than the symbol size.

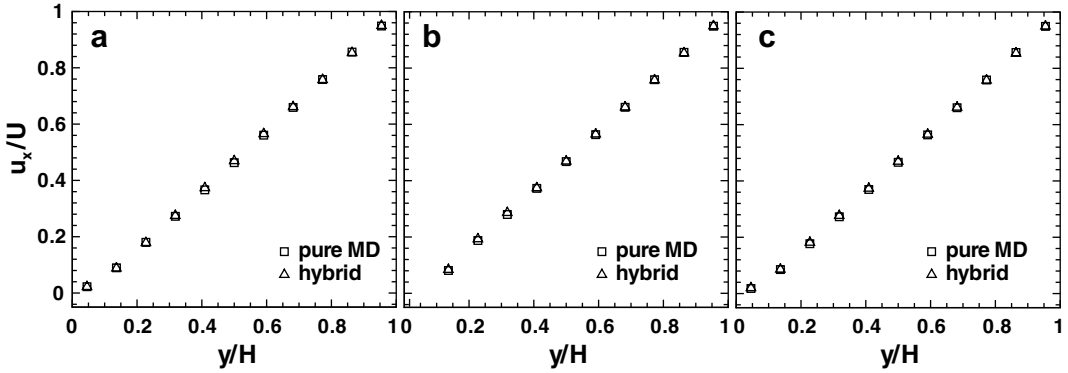

Fig. 6. Comparison of velocity distributions as a function of y at (a) $0.28L_x$, (b) $0.5L_x$ and (c) $0.72L_x$ from hybrid (triangles) and pure MD (squares) simulations for a rough bottom wall and a top wall moving at $U = 1\sigma/\tau$. The results were averaged over 5000τ at steady state and ten independent runs to reduce thermal fluctuations. Errorbars are smaller than the symbol size.

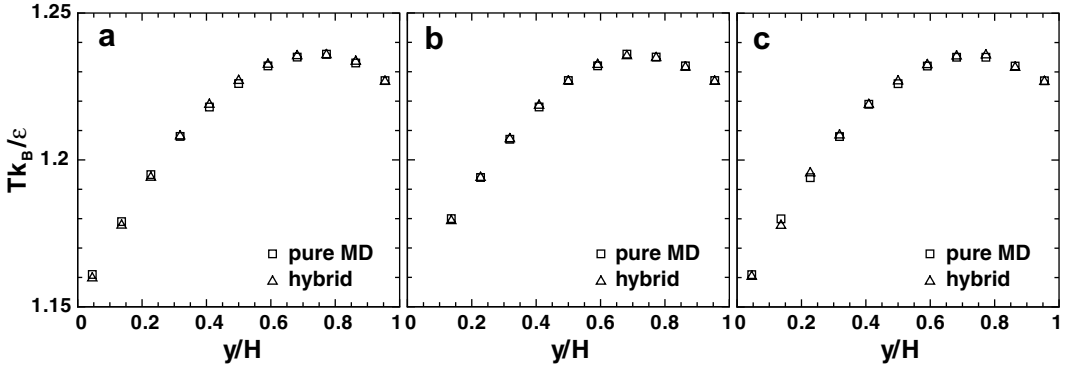

Fig. 7. Comparison of steady state temperature distributions as a function of y at (a) $0.28L_x$, (b) $0.5L_x$ and (c) $0.72L_x$ from hybrid and pure MD simulations for a system with rough bottom wall and top wall moving at $U = 1\sigma/\tau$. The results were averaged over 5000τ at steady state and ten independent runs to reduce thermal fluctuations. Errorbars are smaller than the symbol size.

3.3. Unsteady flow

To test our hybrid method for time dependent heat transfer, we study the transient response to a sudden increase in the temperature of the top wall. The channel height is $H = 112.5\sigma$ and both walls are stationary. Since the temperature drop between the fluid and the top wall is time dependent, it is important to treat both walls atomistically. As shown in Fig. 8, the hybrid simulation contains three domains with MD at top and bottom and continuum in the central region. Pure MD simulations were performed as a reference.

Initially, the simulation was equilibrated for 100τ with the entire system thermostatted at $1.1\epsilon/k_B$. At $t = 0$, the thermostat temperature for the top wall was suddenly raised to $1.2\epsilon/k_B$. The temperature of the fluid was allowed to evolve freely for $t > 0$. The characteristic time for heat to diffuse across the system in continuum theory is of order $t_H = \rho c_v H^2/\lambda = 3235\tau$. The linear steady state profile should be attained at times much longer than t_H. At much shorter times the temperature should follow the solution to the heat equation for an infinite system: $T(y,t) = T_2 - (T_2 - T_1)\Phi[(1 - y/H)\sqrt{t_H/4t}]$, where Φ is the probability integral. The normalized temperature derivative at the top wall should be $h\partial T/\partial y = (T_2 - T_1)\sqrt{t_H/\pi t}$, and the linear fit should

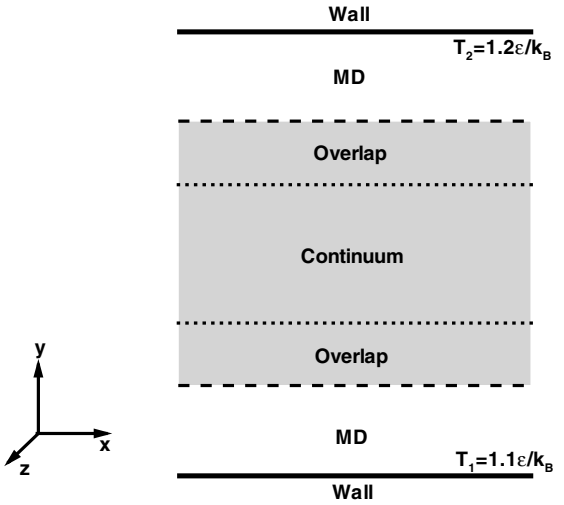

Fig. 8. Schematic of geometry for hybrid simulations of unsteady flow. The continuum description is used in the middle shaded region and the molecular dynamics method is used in both the upper and lower regions.

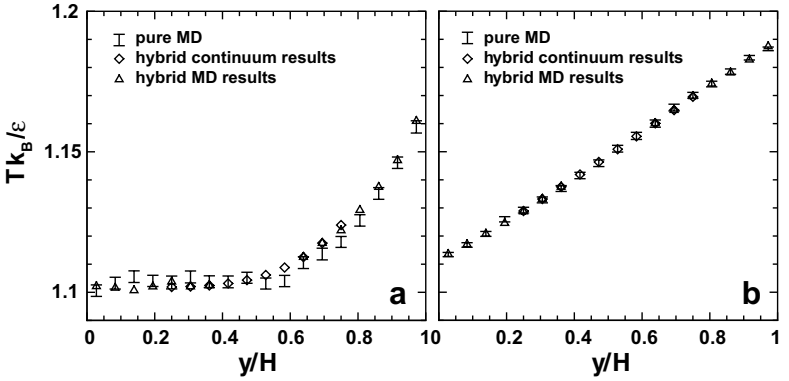

Fig. 9. Comparison of temperature profiles from hybrid and pure MD simulations of a time dependent system. The results were averaged from (a) 100–200τ and (b) 1000–3000τ. The results were averaged over 50 independent runs to reduce thermal fluctuations. Errorbars for the MD simulations are shown, and errorbars for the hybrid simulations are smaller than the symbol size.

reach T_1 at $y/H = 1 - \sqrt{\pi t/t_H}$ Atomistic walls may introduce other time delays associated with the flow of heat from the thermostat to solid atoms and from the solid to the fluid.

Fig. 9a shows the average temperature profile over the time interval from $t = 100\tau$ to 200τ. To improve statistics for this short time interval, both MD and hybrid simulations were averaged over 50 realizations. The two methods are consistent within the errorbars, which are larger for the pure MD simulations. Note that the errors at different y/H are strongly correlated. These correlations were studied by using different ensemble sizes and examining spatio-temporal fluctuations in temperature. These tests show that the spatial correlations result from heat transport in slow hydrodynamic modes. From the continuum solution to the heat equation we would expect the initial slope to extrapolate to zero at about $y/H = 0.62$ for $t = 150\tau$. The actual decay in Fig. 9a is steeper. This indicates that there is an extra delay in heat propagation, presumably due to the heat transfer at the wall/fluid interface. Note that the temperature drop between wall and fluid is very large for these early times. Fig. 9b shows the average profile for t between 1000τ and 3000τ. Agreement between hybrid and pure MD is very good and the errorbars are smaller due to the longer time-averaging interval. Results from both methods are very close to the final steady state solution. This is not surprising, since over this interval the time is larger than t_H/π and thus the continuum estimate for the slope near the wall is more shallow than the steady state solution.

4. Summary and conclusions

Our previous hybrid atomistic/continuum algorithm for incompressible flow [13] has been extended to include heat transfer. MD simulations are used in interfacial regions where atomistic effects are important, while continuum equations are used in bulk regions where fluxes and material properties vary slowly. Both solutions are followed in an overlap region and provide boundary conditions for each other at the outer edges of the overlap region. Continuity of momentum is ensured by "constrained dynamics" that forces the mean atomistic velocity to follow the continuum solution [13]. In this new work, we also include the energy equation. The microscopic temperature is constrained to follow the continuum solution by rescaling the fluctuation of atomistic velocities about the mean. The boundary condition for the continuum solution is determined by the mean microscopic temperature. Maintaining a buffer zone between the locations where these two temperature constraints are applied ensures continuity of heat flux through the overlap region.

The new approach was tested against purely atomistic simulations and analytic solutions. Specific examples included steady state temperature distributions and flow profiles between smooth and rough walls with and without shear. In addition, unsteady temperature distributions in response to a sudden change in wall temperature were examined. In all cases the hybrid method reproduced fully atomistic simulations in a small fraction of the compute time. Of particular importance is the Kapitza resistance at the wall/fluid interface. This atomistic effect was captured in all cases. The results illustrate the potential of our hybrid approach for investigations of heat flow in micro/nano engineering applications, particularly for complex rough walls.

One advantage of the hybrid method is that the number of degrees of freedom that must be integrated is reduced. Most of the computational effort is confined to the interfacial regions that are treated atomistically. These may be an arbitrarily small fraction of the total volume [16]. The size of the continuum region considered in this paper was limited only by the desire to benchmark against purely atomistic results.

A second advantage of the hybrid method over purely atomistic simulations is that thermal fluctuations are reduced. The reason is that thermal fluctuations only enter the small atomistic domain in the hybrid method, while they are generated throughout the entire volume in MD simulations. Removing fluctuations may be undesirable in simulations of processes such as droplet breakup where fluctuations play an intrinsic role. However in many cases one wishes to average out thermal fluctuations to determine the steady state or ensemble average flow and temperature profiles. The hybrid method greatly accelerates such calculations by limiting the size of the region producing fluctuations.

Despite this improvement, the computational effort associated with the hybrid method may still increase rapidly with the size of the continuum region. The reason is that fluctuations in the atomistic region couple to hydrodynamic modes with long time and length scales. These in turn couple back to the atomistic simulation on their characteristic time scales. As a result, averaging must be performed on times longer than the hydrodynamic mode. The effect of thermal fluctuations can be reduced by ensemble averaging results from

the atomistic region before coupling to the continuum equations. Because of the long time scales of hydrodynamic modes, reducing the noise before coupling to the modes is always more efficient than lengthy time averaging.

References

[1] K. Schubert, J. Brandner, M. Fichtner, G. Linder, U. Schygulla, A. Wenka, Microstructure devices for applications in thermal and chemical process engineering, Microscale Thermophys. Eng. 5 (2001) 17–39.
[2] T. Kunugi, K. Muko, M. Shibahara, Ultrahigh heat transfer enhancement using nano-porous layer, Superlattices Microstruct. 35 (2004) 531–542.
[3] T. Bayraktar, S.B. Pidugu, Characterization of liquid flows in microfluidic systems, Int. J. Heat Mass Transf. 49 (2006) 815–824.
[4] S.T. O'Connell, P.A. Thompson, Molecular dynamics–continuum hybrid computations: a tool for studying complex fluid flows, Phys. Rev. E 52 (1995) R5792–R5795.
[5] N.G. Hadjiconstantinou, A.T. Patera, Heterogeneous atomistic–continuum representations for dense fluid systems, Int. J. Mod. Phys. C 8 (1997) 967–976.
[6] N.G. Hadjiconstantinou, Hybrid atomistic–continuum formulations and the moving contact-line problem, J. Comput. Phys. 154 (1999) 245–265.
[7] E.G. Flekkoy, G. Wagner, J. Feder, Hybrid model for combined particle and continuum dynamics, Europhys. Lett. 52 (2000) 271–276.
[8] G. Wagner, E.G. Flekkoy, J. Feder, T. Jossang, Coupling molecular dynamics and continuum dynamics, Comput. Phys. Commun. 147 (2002) 670–673.
[9] G. Wagner, E.G. Flekkoy, Hybrid computations with flux exchange, Philos. Trans. Roy. Soc. London A 362 (2004) 1655–1665.
[10] R. Delgado-Buscalioni, P.V. Coveney, Continuum-particle hybrid coupling for mass, momentum and energy transfers in unsteady fluid flow, Phys. Rev. E 67 (2003) 046704-1–046704-13.
[11] R. Delgado-Buscalioni, P.V. Coveney, Hybrid molecular-continuum fluid dynamics, Philos. Trans. Roy. Soc. London A 362 (2004) 1639–1654.
[12] E.G. Flekkoy, R. Delgado-Buscalioni, P.V. Coveney, Flux boundary conditions in particle simulations, Phys. Rev. E 72 (2005) 026703.
[13] X.B. Nie, S.Y. Chen, W. E, M.O. Robbins, A continuum and molecular dynamics hybrid method for micro- and nano-fluid flow, J. Fluid Mech. 500 (2004) 55–64..
[14] X.B. Nie, S.Y. Chen, M.O. Robbins, Hybrid continuum–atomistic simulation of singular corner flow, Phys. Fluids 16 (2004) 3579–3591.
[15] W. Ren, W. E, Heterogeneous multiscale method for modeling of complex fluids and micro-fluidics, J. Comput. Phys. 204 (2005) 1–26.
[16] X.B. Nie, M.O. Robbins, S.Y. Chen, Resolving singular forces in cavity flow: multiscale modeling from atomic to millimeter scales, Phys. Rev. Lett. 96 (2006) 134501.
[17] G.S. Grest, K. Kremer, Molecular dynamics simulation for polymers in the presence of a heat bath, Phys. Rev. A 33 (1986) 3628–3631.
[18] R. Peyret, T.D. Taylor, Computational Methods for Fluid Flow, Springer, 1983.
[19] M. Moseler, U. Landman, Formation, stability and breakup of nanojets, Science 289 (2005) 1165–1169.
[20] T. Werder, J.H. Walther, P. Koumoutsakos, Hybrid atomistic–continuum method for the simulation of dense fluid flows, J. Comput. Phys. 205 (2005) 373–390.
[21] M.P. Allen, D.J. Tildesley, Computer Simulation of Liquids, Clarendon Press, Oxford, 1987.
[22] J.M. Haile, Molecular Dynamics Simulation: Elementary Methods, John Wiley, Chichester, 1997.
[23] F. Muller-Plathe, A simple nonequilibrium molecular dynamics method for calculating the thermal conductivity, J. Chem. Phys. 106 (1997) 6082–6085.
[24] P.L. Kapitza, The study of heat transfer in helium II, Zh. Eksp. Teor. Fiz. 11, 1 [J. Phys. (USSR) 4 (1941) 181].
[25] E.T. Swartz, R.O. Pohl, Thermal boundary resistance, Rev. Mod. Phys. 61 (1989) 605–668.
[26] R. Khare, J.J. de Pablo, A. Yethiraj, Rheology of confined polymer melts, Macromolecules 29 (1996) 7910–7918.